

Networked Sensing with AI-Empowered Environment Estimation: Exploiting Macro-Diversity and Array Gain in Perceptive Mobile Networks

Lei Xie and S.H. Song

Abstract

Sensing will be an important service for future wireless networks to assist innovative applications like autonomous driving and environment monitoring. This paper considers the design of perceptive mobile networks (PMNs) where target monitoring terminals (TMTs) are deployed over the traditional cellular networks for jointly sensing the targets in the presence of environment clutter. Different from traditional radar, the cellular structure of PMNs offers multiple perspectives for target sensing (TS), but the joint processing among distributed sensing nodes also causes heavy computation and communication workload over the network. In this paper, we first propose a two-stage protocol where communication signals are utilized for environment estimation (EE) and TS in two consecutive time periods, respectively. A *networked* sensing detector is then derived to exploit the perspectives provided by multiple TMTs for sensing the same target. The macro-diversity from multiple TMTs and the array gain from multiple receive antennas at each TMT are analyzed to reveal the benefit of networked sensing. Furthermore, we derive the sufficient condition that one TMT's contribution to the networked sensing is positive, based on which a TMT selection algorithm is proposed. To reduce the computation burden and efficiently estimate the environment, we propose a model-driven deep-learning algorithm that utilizes partially-sampled data for EE. Simulation results confirm the benefits of networked sensing and validate the higher efficiency of the proposed EE algorithm than existing methods.

Index Terms

L. Xie and S.H. Song are with Department of Electronic and Computer Engineering, the Hong Kong University of Science and Technology, Hong Kong. e-mail: ({eelixie,eeshsong}@ust.hk).

Perceptive mobile network, integrated sensing and communication, macro-diversity, array gain, unfolding deep networks.

I. INTRODUCTION

With the development of innovative applications such as autonomous driving and industrial internet of things (IoT) [1]–[3], there is an increasing demand on sensing services such as target tracking and environmental monitoring [4], [5]. Unfortunately, the current mobile networks, though very successful in providing communication services, are not able to meet the accurate sensing requirement of the above applications. To this end, the recently proposed integrated sensing and communication (ISAC) framework provides a promising platform to integrate sensing capability into wireless communication systems [6], [7], where perceptive mobile networks (PMNs) were proposed by adding sensing ability to current cellular networks.

There are many favorable properties of mobile networks that can facilitate sensing. First, the well developed cellular networks can provide large surveillance coverage. Second, the high-density and multiple-antenna nodes, such as base stations (BSs), not only offer sufficient spatial freedom for interference cancellation, but also enables networked sensing. Finally, the strong computation and communication power of the network provides a good platform for environment estimation (EE), which is critical for radar sensing. However, there are also new challenges. For example, the integration of sensing and communication requires proper interference management and resource allocation between the two systems in both device (full-duplex operation [8]) and network level (multi-user interference [9]). Furthermore, the sensing environment for PMNs is much more complex than traditional radar due to abundant signal blockages and environment clutter, making both EE and target sensing (TS) difficult. Finally, the networked sensing with multiple distributed nodes may cause heavy communication and computation workload over the network.

Interference management and resource allocation are at the core of ISAC network design. In the system level, there exists the interference between communication and sensing users, which needs to be properly handled. On the other hand, utilizing BSs to serve communication users and sense targets at the same time will cause self-interference and require the full-duplex operation. Some research efforts have been made on self-interference cancellation (SIC) [10], [11] to enable the full-duplex operation, which unfortunately is still immature. [12] proposed a framework for resource allocation in dual-functional BS by optimizing a novel metric, i.e.,

sensing quality of service (QoS). An ISAC network based on multiple unmanned aerial vehicles (UAVs) was proposed in [13], where the communication performance was optimized with a given sensing performance by jointly designing the UAV locations, user association, and UAV transmission power. In these works, the BSs/UAVs were required to work in the full-duplex mode. [5] addressed the full-duplex issue by deploying some radio remote units (RRUs) as sensing receivers in a cloud radio access network (C-RAN). Along the same line of research, [14] proposed to utilize another layer of passive target monitoring terminals (TMTs) to save the need for the full-duplex operation. However, the networked sensing with multiple nodes, e.g., RRUs, UAVs, or TMTs, has not been well investigated.

Another challenge for PMNs is EE. To achieve good sensing performance in the presence of clutter, PMNs need to suppress the clutter by utilizing the prior information about the environment obtained by EE. The performance of clutter suppression will degrade if the clutter component of the signal under test has different statistical structure from that of the training data. [15] proposed a compressed sensing (CS)-based method to estimate the spatial parameters and Doppler shift of the clutter. Unfortunately, the computational cost of the CS-based method can be extremely high, due to the continuous and rapidly-changing environment parameters in the space and Doppler domains. This issue will be more serious when multiple distributed nodes are involved in the networked sensing where information sharing between different nodes are necessary. Thus, a computation and communication efficient EE algorithm is desired.

In this paper, we consider the PMN where another layer of target monitoring terminals (TMTs) are deployed for sensing purpose so that the full-duplex operation is not needed. In particular, the TMTs are passive nodes with only perception functionalities, including radar, vision, and other sensing capabilities [3], [16]. They are distributed in a target area and connected with the base stations (BSs) through low latency links. As a result, BSs will also serve as radar transmitters besides performing their communication duty and the sensing task is jointly performed by the TMTs instead of the dual-functional BSs to avoid the full-duplex operation.

We first propose a two-stage protocol where EE and TS are performed in two consecutive periods, respectively, by utilizing communication signals. In order to guarantee the environment statistics donot change in the TS period, the sensing signal is properly designed to avoid affecting the clutter. We then derive a networked detector based on the generalized likelihood ratio test (GLRT) detection, which is optimal in terms of maximizing the signal-to-clutter-plus-noise ratio (SCNR). Performance evaluation is then performed to reveal the impact of several key system

parameters, including the number of TMTs and the number of antennas at the TMT. Physical insights with respect to the macro-diversity and array gain are then revealed, identifying unique advantages of the networked sensing.

To reduce the computation and communication workload for EE, we further propose a distributed clutter covariance estimation algorithm where the estimation is performed at TMTs. The low rank clutter [17]–[19] makes it possible to estimate the clutter covariance by using partial samples of the received signal. However, the estimated covariance matrix may be ill-conditioned due to the limited data samples. To this end, we propose the EM-Net algorithm by unfolding the expectation-maximization (EM) detector with several learnable parameters, which achieves accurate estimation with less data than existing methods.

The contributions of this paper can be summarized as follows:

- 1) We propose a two-stage protocol for sensing the target in the presence of environment clutter, where the communication signals are utilized for EE and TS. To ensure the clutter component in the signal under test has the same statistical structure as the estimated clutter, the precoder for sensing signal is designed not to affect the clutter patches in the environment.
- 2) We derive a networked detector where multiple TMTs collaboratively sense a target with a constant false alarm probability. We theoretically evaluate the performance of the proposed detector, whose accuracy is validated by simulation.
- 3) The impact of the number of TMTs and the number of antennas at the TMTs are investigated. For the former, we derive the sufficient condition for the contribution of one TMT to be positive and propose a TMT selection algorithm based on the condition. For the latter, we show that, different from communication, multiple antennas only provide array gain but no diversity gain in sensing, due to the use of only the LoS component.
- 4) To improve the computation and communication efficiency, we propose an efficient EE method by unfolding the EM method where several learnable parameters are introduced. Compared with the existing method, the proposed method can achieve better estimation performance with less data.

The remainder of this paper is organized as follows. Section II introduces the system model and the two-stage protocol. Section III proposes the networked detector and evaluates the performance of the proposed detector. The impact of the key parameters, including the number of TMTs (macro-diversity) and number of antennas (array gain) are also investigated. Section IV introduces

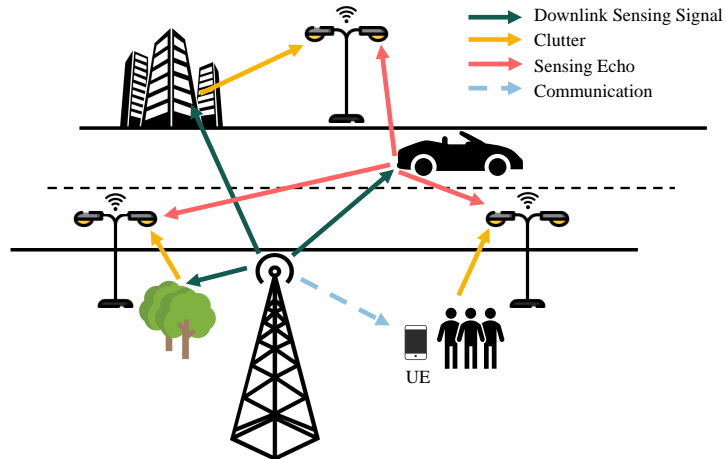


Fig. 1. Illustration of system structure.

an efficient AI-empowered EE algorithm. Section V validates the performance of the proposed detector and the accuracy of the proposed algorithm by simulation results.

II. SYSTEM MODEL AND TWO-STAGE SENSING

Consider a PMN where passive TMTs are implemented over the conventional cellular networks for sensing purpose, as illustrated in Fig. 1. Assume that the BSs and TMTs are equipped with N_T and N_R antennas, respectively. The objective in this paper is to detect whether a target is present at a given location. Note that the adding of the TMTs saves the need for the full-duplex operation. However, the protocol and networked detector proposed in this paper are valid for other PMN infrastructure, such as those using full-duplex BSs and RRUs for sensing.

In order to achieve radar sensing without disturbing the communication users, we propose a two-stage protocol as illustrated in Fig. 2. Note that the normal communication service is not affected by sensing, which only happens in the downlink period. In particular, the downlink period is divided into two periods, i.e., the EE period and TS period. During the EE period, BSs not only serve the communication users but also send radar signal for EE, while the radar detection is jointly achieved by multiple TMTs in the TS period also based on communication signals. In the following, we explain the detailed operations of the two periods, respectively.

A. Communication and EE Period

In this period, we assume the target is absent. The BSs will send the communication signals to the UEs, which will be reflected by the environment and captured by the TMTs for EE.

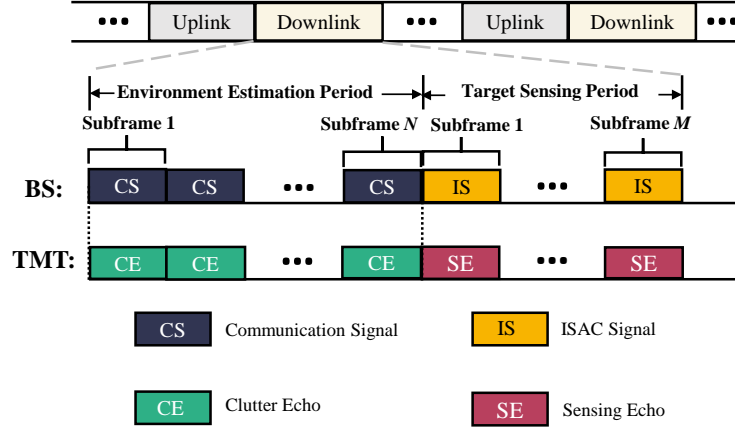


Fig. 2. Frame structure for the proposed integrated sensing and communication protocol.

Specifically, in the n th subframe, the BS transmits communication signals to K UEs and the received signal at the l th TMT is given as [20], [21]

$$\mathbf{y}_{c,l}(n) = \mathbf{H}_l(n)\mathbf{F}\mathbf{s}(n) + \mathbf{n}_l(n), n = 1, 2, \dots, N, \quad (1)$$

where $\mathbf{s}(n) \in \mathbb{C}^{K \times 1}$ denotes the communication signal with covariance matrix \mathbf{I} , $\mathbf{F} \in \mathbb{C}^{N_T \times K}$ represents the precoder matrix, and $\mathbf{n}_l(n)$ is the additive white Gaussian noise (AWGN) with zero mean and covariance matrix $\sigma^2\mathbf{I}$. Note that $\mathbf{F}\mathbf{s}(n)$ and $\mathbf{y}_{c,l}(n)$ correspond to the ‘‘Communication Signal’’ and ‘‘Clutter Echo’’ in Fig. 2, respectively. Here, $\mathbf{H}_l(n) \in \mathbb{C}^{N_R \times N_T}$ denotes the channel matrix between the BS and the l th TMT. With uniform linear array, the steering vector of the BS with angle of departure (AOD) ϕ and that of the l th TMT with angle of arrive (AOA) θ are respectively defined as

$$\mathbf{a}_T(\phi) = \frac{1}{\sqrt{N_T}} \left[1, e^{j2\pi\frac{d}{\lambda}\cos\phi}, \dots, e^{j2\pi(N_T-1)\frac{d}{\lambda}\cos\phi} \right]^T \in \mathbb{C}^{N_T \times 1}, \quad (2)$$

$$\mathbf{a}_R(\theta) = \frac{1}{\sqrt{N_R}} \left[1, e^{j2\pi\frac{d}{\lambda}\cos\theta}, \dots, e^{j2\pi(N_R-1)\frac{d}{\lambda}\cos\theta} \right]^T \in \mathbb{C}^{N_R \times 1}, \quad (3)$$

where d is the antenna spacing and λ represents the wave length. Thus, the channel matrix with P clutter patches is defined as

$$\mathbf{H}_l(n) = \sqrt{N_R N_T} \sum_{i=1}^P \epsilon_{l,i}(n) \mathbf{a}_R(\theta_{l,i}) \mathbf{a}_T^H(\phi_i) \in \mathbb{C}^{N_R \times N_T}, \quad (4)$$

where $\epsilon_{l,i}(n)$ denotes the channel coefficient of the i th clutter patch observed by the l th TMT, which is assumed to follow a complex Gaussian distribution with zero mean and variance $\sigma_{l,i}^2$

[22]. ϕ_i denotes the AOD from BS to the i th clutter patch and $\theta_{l,i}$ represents the AOA from i th clutter patch to the l th TMT. Here, we omit the paths reflected more than one time. These P clutter patches come from two sources: 1) the strong scatter points¹, and 2) the UEs. Note that the reflecting coefficient of the UEs may be low, but the transmit power towards the UEs is high. Therefore, the echoes from the UEs can not be neglected. Note that $\mathbf{y}_{c,l}(n), n = 1, 2, \dots, N$ are independent and identically distributed (i.i.d) with respect to n . For ease of illustration, we rewrite (1) as

$$\mathbf{y}_{c,l}(n) = \mathbf{A}_{R,l}\mathbf{t}_l(n) + \mathbf{n}_l(n), n = 1, 2, \dots, N, \quad (5)$$

where

$$\mathbf{A}_{R,l} = [\mathbf{a}_R(\theta_{l,1}), \dots, \mathbf{a}_R(\theta_{l,P})] \in \mathbb{C}^{N_R \times P},$$

$$\mathbf{t}_l(n) = \left[\sqrt{N_R N_T \epsilon_{l,1}}(n) \mathbf{a}_T^H(\phi_1) \mathbf{F} \mathbf{s}(n), \dots, \sqrt{N_R N_T \epsilon_{l,P}}(n) \mathbf{a}_T^H(\phi_P) \mathbf{F} \mathbf{s}(n) \right]^T \in \mathbb{C}^{P \times 1}.$$

It can be validated that the $\mathbf{y}_{c,l}(n)$ follows the Gaussian distribution with $\mathbf{y}_{c,l}(n) \sim \mathcal{CN}(\mathbf{0}, \mathbf{R}_{c,l}), n = 1, \dots, N$, where

$$\mathbf{R}_{c,l} \triangleq \mathbb{E} \{ \mathbf{y}_{c,l}(n) \mathbf{y}_{c,l}^H(n) \} = \underbrace{\mathbf{A}_{R,l} \mathbf{P}_l \mathbf{A}_{R,l}^H}_{\text{Environment}} + \underbrace{\sigma^2 \mathbf{I}}_{\text{Noise}}, \quad (6)$$

and $\mathbf{P}_l = \text{Diag} \left([\sqrt{N_R N_T} \sigma_{l,1}^2 |\mathbf{a}_T^H(\phi_1) \mathbf{F}|^2, \dots, \sqrt{N_R N_T} \sigma_{l,P}^2 |\mathbf{a}_T^H(\phi_P) \mathbf{F}|^2] \right)$. The main task of the TMTs in this period is to estimate the clutter covariance matrix $\mathbf{R}_{c,l}$ based on the samples $\mathbf{y}_{c,l}(n), n = 1, \dots, N$.

B. Communication and TS Period

In the TS period, the system aims to probe a target without influencing the communication performance. The target is assumed to be point-like and static or slow moving, which is also known as the Swerling I model [23], where the Doppler effect is neglected. To achieve a good sensing performance, the received clutter in the TS period is supposed to have the same second-order statistics as that in the EE period. For that purpose, we need to properly design the precoder. Define

$$\mathbf{A}_T = [\mathbf{a}_T(\phi_1), \dots, \mathbf{a}_T(\phi_P)], \quad (7)$$

¹They include the building shown in Fig. 1 and the line-of-sight (LOS) between the BS and TMTs, if any.

where the positions of the clutter patches, i.e., $\{\phi_i\}_{i=1}^P$, are known from the EE period. To make sure the second order statistics of the echo signals do not change in the TS period, we need to guarantee that the sounding signal toward the sensing target, with AoD ϕ_t ², will not create echoes by the clutter patches. For that purpose, we construct \mathbf{f}_\perp as the projection of $\mathbf{a}_T(\phi_t)$ in the null-space of \mathbf{A}_T , i.e.,

$$\mathbf{f}_\perp = \frac{\mathbf{a}_T(\phi_t) - \mathbf{A}_T(\mathbf{A}_T^H \mathbf{A}_T)^{-1} \mathbf{A}_T^H \mathbf{a}_T(\phi_t)}{1 - \mathbf{a}_T^H(\phi_t) \mathbf{A}_T(\mathbf{A}_T^H \mathbf{A}_T)^{-1} \mathbf{A}_T^H \mathbf{a}_T(\phi_t)}. \quad (8)$$

It can be validated that $\mathbf{A}_T^H \mathbf{f}_\perp = \mathbf{0}$, i.e., \mathbf{f}_\perp will not affect the response on the direction of clutter patches. It has been shown in [14] that redesigning communication signals for sensing is more efficient than creating a dedicated sensing signal. Thus, we create the precoder in the TS period as

$$\mathbf{F}_{\text{ISAC}} = \mathbf{F} + \mathbf{f}_\perp \boldsymbol{\omega}^T, \quad (9)$$

where $\boldsymbol{\omega} = [\omega_1, \omega_2, \dots, \omega_K]^T$ denotes the weights corresponding to different data streams. Here,

$$\mathbf{F}_{\text{ISAC}} \mathbf{s} = \mathbf{F} \mathbf{s} + \mathbf{f}_\perp \boldsymbol{\omega}^T \mathbf{s} \quad (10)$$

corresponds to the ‘‘ISAC Signal’’ in Fig. 2. Note that, compared with the transmit signal in the EE period, the additional signal $\mathbf{f}_\perp \boldsymbol{\omega}^T \mathbf{s}$ will not create echos from the clutter patches, including the UEs. This guarantees that the communication performance will not be affected by sensing and the environment covariance structure is the same in the EE and TS periods.

Here, we only consider one subframe in the TS period and the result can be extended to the case with more subframes. Thus, the received signal at the l th TMT in the TS period is given as

$$\begin{aligned} \mathbf{y}_{s,l} &= \left(\mathbf{H}_l + \sqrt{N_R N_T} \epsilon_{t,l} \mathbf{a}_R(\theta_{t,l}) \mathbf{a}_T^H(\phi_t) \right) \mathbf{F}_{\text{ISAC}} \mathbf{s} + \mathbf{n}_l \\ &= c_{t,l} \mathbf{a}_R(\theta_{t,l}) + \mathbf{A}_{R,l} \mathbf{t}_l + \mathbf{n}_l, \end{aligned} \quad (11)$$

where $\theta_{t,l}$ denotes the AOA of target at the l th TMT, and

$$c_{t,l} = \sqrt{N_R N_T} \epsilon_{t,l} \mathbf{a}_T^H(\phi_t) \mathbf{F}_{\text{ISAC}} \mathbf{s} = \sqrt{N_R N_T} \epsilon_{t,l} \left(\mathbf{a}_T^H(\phi_t) \mathbf{F} \mathbf{s} + \sum_{k=1}^K \omega_k s_k \right), \quad (12)$$

represents the complex amplitude of the target component with $\epsilon_{t,l}$ denoting the channel coefficient of the BS-target-TMT (l th) link. We assume that $\epsilon_{t,l}$ does not change in one TS subframe.

²We assume that $\phi_t \neq \phi_i, \forall i$, because otherwise the target can not be detected.

Note that $\mathbf{y}_{s,l}$ corresponds to the ‘‘Sensing Echo’’ in Fig. 2 and the first term in (11) represents the echo from the target.

It follows from (11) that $\mathbf{y}_{s,l}$ follows the Gaussian distribution with $\mathbf{y}_{s,l} \sim \mathcal{CN}(c_{t,l}\mathbf{a}_R(\theta_{t,l}), \mathbf{R}_{s,l})$, where

$$\mathbf{R}_{s,l} \triangleq \mathbb{E} \left\{ (\mathbf{y}_{s,l} - c_{t,l}\mathbf{a}_R(\theta_{t,l})) (\mathbf{y}_{s,l} - c_{t,l}\mathbf{a}_R(\theta_{t,l}))^H \right\} = \mathbf{A}_{R,l} \mathbf{P}_l \mathbf{A}_{R,l}^H + \sigma^2 \mathbf{I}. \quad (13)$$

Comparing (6) and (13), we can observe that the clutter in the TS period has the same covariance matrix as that in the EE period. Without loss of generality, we denote $\mathbf{R}_{c,l} = \mathbf{R}_{s,l} = \mathbf{R}_l$.

III. NETWORKED SENSING WITH MULTIPLE TMTs

The distributed TMTs provide multiple perspectives to observe the target. In this section, we propose a networked detector and then evaluate its performance to reveal some physical insights for system design.

A. Networked Sensing

Radar detection is a binary hypothesis testing problem, where hypotheses \mathcal{H}_0 and \mathcal{H}_1 correspond to the absence and presence of the target, respectively, i.e.,

$$\begin{aligned} \mathcal{H}_0 : \mathbf{y}_l &\sim \mathcal{CN}(\mathbf{0}, \mathbf{R}_l) \\ \mathcal{H}_1 : \mathbf{y}_l &\sim \mathcal{CN}(c_{t,l}\mathbf{a}_R(\theta_{t,l}), \mathbf{R}_l) \end{aligned} \quad (14)$$

with \mathbf{y}_l denoting the data under test at the l th TMT in the TS period. Given the echo signals received by different TMTs are independent due to the independent reflecting coefficients, the optimal detector that maximizes the output signal-to-clutter-plus-noise ratio (SCNR) is the generalized likelihood ratio test (GLRT) detector [24], i.e.,

$$\Gamma = \sum_{l=1}^L \Gamma_l \underset{\mathcal{H}_0}{\overset{\mathcal{H}_1}{\geq}} \gamma_L, \quad (15)$$

where γ_L denotes the detection threshold and

$$\Gamma_l \triangleq \frac{|\mathbf{a}_R^H(\theta_{t,l}) \mathbf{R}_l^{-1} \mathbf{y}_l|^2}{\mathbf{a}_R^H(\theta_{t,l}) \mathbf{R}_l^{-1} \mathbf{a}_R(\theta_{t,l})}. \quad (16)$$

For ease of illustration, we will utilize $\mathbf{a}_{t,l}$ to denote $\mathbf{a}_R(\theta_{t,l})$. Under \mathcal{H}_0 , the data-under-test only contains clutter and noise. Thus, the detection statistic Γ_l in (16) follows a central chi-square distribution with 2 degrees of freedom (DOF), i.e., $\Gamma_l \sim \chi_2^2(0)$. Under \mathcal{H}_1 , the detection

statistic Γ_l follows a chi-square distribution with 2 degrees of freedom (DOF) and non-central parameter μ_l^2 , i.e., $\Gamma_l \sim \chi_2^2(\mu_l^2)$, where $\mu_l^2 = c_{t,l}^2 \mathbf{a}_{t,l}^H \mathbf{R}_l^{-1} \mathbf{a}_{t,l}$. Thus, we have

$$\Gamma = \sum_{l=1}^L \Gamma_l \sim \begin{cases} \chi_{2L}^2(\zeta_L), & \mathcal{H}_1, \\ \chi_{2L}^2(0), & \mathcal{H}_0, \end{cases} \quad (17)$$

where $\zeta_L = \sum_{l=1}^L \mu_l^2$ is the non-central parameter of chi-square decision statistic.

Following the result in [25], the false alarm probability is given by

$$P_{fa} = e^{-\frac{\gamma_L}{2}} \sum_{l=0}^{L-1} \frac{\left(\frac{\gamma_L}{2}\right)^l}{l!}, \quad (18)$$

indicating that P_{fa} is dependent on γ_L and L , but independent with the clutter covariance $\{\mathbf{R}_l\}$.

The decision threshold can be determined without prior knowledge of the environment, i.e., [26]

$$\gamma_L \approx \left(L - \frac{1}{2}\right) + \left(\sqrt{-\frac{8}{5} \ln(4P_{fa}(1 - P_{fa}))} + \sqrt{L - \frac{1}{2}}\right)^2 \quad (19)$$

which is also known as the constant false alarm rate (CFAR) property [23], [24]. This property improves the robustness of the system. Finally, the detection probability can be written as [27]

$$P_d^{(L)} = Q_L\left(\sqrt{\zeta_L}, \sqrt{\gamma_L}\right) = Q_L\left(\sqrt{\sum_{l=1}^L c_{t,l}^2 \mathbf{a}_{t,l}^H \mathbf{R}_l^{-1} \mathbf{a}_{t,l}}, \sqrt{\gamma_L}\right), \quad (20)$$

where $Q_k(\cdot, \cdot)$ denotes the generalized Marcum Q function of order k. In the following, we analyze the impact of two most important system parameters, namely, the number of antennas at each TMT and the number of TMTs participating in the joint sensing.

B. Array Gain: Impact of multiple antennas in one TMT

In this section, we will discuss the contribution of one TMT through analyzing μ_l^2 . For that purpose, we first perform the eigen-decomposition on \mathbf{R}_l with

$$\mathbf{R}_l = \mathbf{R}_l + \sigma^2 \mathbf{I} = \mathbf{V}_l \mathbf{\Lambda}_l \mathbf{V}_l^H + \sigma^2 \mathbf{I}, \quad (21)$$

where $\mathbf{V}_l = [\mathbf{v}_{l,1}, \dots, \mathbf{v}_{l,P}] \in \mathbb{C}^{N_R \times P}$, $\mathbf{\Lambda}_l = \text{Diag}(\lambda_{l,1}, \dots, \lambda_{l,P})$. Therefore, we have

$$\mathbf{R}_l^{-1} = (\mathbf{V}_l \mathbf{\Lambda}_l \mathbf{V}_l^H + \sigma^2 \mathbf{I})^{-1} = \frac{1}{\sigma^2} (\mathbf{I} - \mathbf{V}_l (\sigma_n^2 \mathbf{\Lambda}_l^{-1} + \mathbf{V}_l^H \mathbf{V}_l)^{-1} \mathbf{V}_l^H), \quad (22)$$

where we have used the matrix inversion lemma. For a relatively high clutter to noise ratio (CNR) [28], [29], i.e., $\lambda_{l,i} \gg \sigma^2$, we have

$$\mu_l^2 = c_{t,l}^2 \mathbf{a}_{t,l}^H \mathbf{R}_l^{-1} \mathbf{a}_{t,l} \approx \frac{c_{t,l}^2}{\sigma^2} \|\mathbf{P}_{V,l}^\perp \mathbf{a}_{t,l}\|^2 = \text{SNR}_l \cdot \cos^2 \vartheta_{tv,l}^\perp, \quad (23)$$

where $\text{SNR}_l \triangleq \frac{c_{t,l}^2}{\sigma^2}$ denotes the signal-to-noise ratio (SNR) at the l th TMT. Here, $\mathbf{P}_{V,l}^\perp = \mathbf{I} - \mathbf{V}_l(\mathbf{V}_l^H \mathbf{V}_l)^{-1} \mathbf{V}_l^H$ denotes the projector onto the null space of $\text{span}(\mathbf{V}_l)$, and $\vartheta_{tv,l}^\perp$ represents the angle between $\mathbf{P}_{V,l}^\perp \mathbf{a}_{t,l}$ and $\mathbf{a}_{t,l}$. We can rewrite SNR_l [22]

$$\text{SNR}_l = \frac{C_g N_R P_T}{r_l^\beta}, \quad (24)$$

where C_g is a constant related to the noise variance and antenna gains, P_T is the transmission power, r_l denotes the length of the BS-target-TMT link for the l -th TMT, and β is the path loss exponent. Meanwhile, we have $\cos^2(\vartheta_{tv,l}^\perp) = 1 - \cos^2(\vartheta_{tv,l}) = 1 - |\mathbf{a}_{t,l}^H \mathbf{a}_{p,l}|$, where $\mathbf{a}_{p,l} \triangleq \mathbf{P}_{V,l} \mathbf{a}_{t,l}$ denotes the orthogonal projection of $\mathbf{a}_{t,l}$ onto $\text{span}(\mathbf{V}_l)$. According to (6), we have $\text{span}(\mathbf{V}_l) = \text{span}(\mathbf{A}_{R,l})$. Then, there exists a set of positive weight $\{\alpha_{i,l} \in [0, 1]\}$, such that $\mathbf{a}_{p,l} = \sum_{i=1}^P \alpha_{i,l} \mathbf{a}_R(\theta_{l,i})$. It thus follows from (3) that

$$\begin{aligned} |\mathbf{a}_{t,l}^H \mathbf{a}_{p,l}| &= \frac{1}{N_R} \left| \sum_{i=1}^P \sum_{n=1}^{N_R} \alpha_{i,l} e^{j2\pi(n-1)\frac{d}{\lambda}(\cos \theta_{t,l} - \cos \theta_{l,i})} \right| \\ &= \frac{1}{N_R} \left| \sum_{i=1}^P \alpha_{i,l} \frac{e^{j\pi N_R \frac{d}{\lambda}(\cos \theta_{t,l} - \cos \theta_{l,i})} \sin\left(\pi N_R \frac{d}{\lambda}(\cos \theta_{t,l} - \cos \theta_{l,i})\right)}{e^{j\pi \frac{d}{\lambda}(\cos \theta_{t,l} - \cos \theta_{l,i})} \sin\left(\pi \frac{d}{\lambda}(\cos \theta_{t,l} - \cos \theta_{l,i})\right)} \right|, \end{aligned} \quad (25)$$

where we have utilized the Euler's identity, i.e., $2j \sin \theta = e^{j\theta} - e^{-j\theta}$.

Substituting (24) and (25) into (23) yields

$$\mu_l^2 \approx \frac{C_g N_R P_T}{r_l^\beta} \left(1 - \left| \sum_{i=1}^P \alpha_{i,l} e^{j\pi(N_R-1)\frac{d}{\lambda}(\cos \theta_{t,l} - \cos \theta_{l,i})} \frac{\text{sinc}(N_R \Delta_{l,i})}{\text{sinc}(\Delta_{l,i})} \right| \right) \quad (26)$$

where $\text{sinc}(x) = \frac{\sin \pi x}{\pi x}$ and $\Delta_{l,i} = \frac{d}{\lambda}(\cos \theta_{t,l} - \cos \theta_{l,i})$.

Remark 1: It can be observed from (26) that the contribution of the l th TMT is determined by several parameters.

- 1) The length of the BS-Target-TMT link, r_l , affects the SNR exponentially.
- 2) The relation between $\theta_{t,l}$ and $\{\theta_{l,i}\}_{i=1}^P$ affects the ability of the l th TMT to reject the clutter. To obtain a larger μ_l^2 , we want the summation in (26) to be small. As a result, $\theta_{t,l}$ and $\theta_{l,i}$ are preferred to be far apart, i.e., a TMT with ‘‘clearer’’ view of the taret is preferred.
- 3) The number of antennas at the TMT has two effects. On the one hand, SNR_l is directly proportional to N_R , which comes from the antenna array gain. On the other hand, $\cos \vartheta_{tv,l}$ also depends on N_R , which is referred to as the resolution of the TMT. In particular, the mainlobe of $\text{sinc}(N_R \Delta)$ can be obtained by setting $\pi N_R \Delta = \pi$, which gives the boundary of the mainlobe at $\Delta_{ml} = \frac{1}{N_R}$. For the considered ULA, $\text{sinc}(N_R \Delta)$ is approximately 13 dB down from the peak of the mainlobe when Δ is out of $(-\Delta_{ml}/2, \Delta_{ml}/2)$. Since $\theta_{t,l}$

and θ_l are fixed, Δ_{ml} will decrease as N_R increases and the mainlobe of $\text{sinc}(N_R\Delta)$ will become narrower, leading to a larger μ_l^2 .

Remark 2: The impact of multiple antennas in sensing is different from that in communication. For instance, multiple antennas can offer both diversity and multiplexing gain in wireless channels. However, for sensing, only the LOS component is utilized and the NLOS components are regarded as part of the clutter. As a result, no diversity gain is provided by multiple receive antennas in sensing applications and Γ_l in (16) only has one complex DOF. However, a larger number of antennas does provide higher array gain and better interference rejection ability, which leads to larger SNR_l and $\cos^2 \vartheta_{lv,l}^\perp$, respectively.

C. Macro-diversity: Contribution of multiple TMTs

In this section, we discuss the benefit of networked sensing.

1) *Impact of the number of TMTs:* It follows from (20) that the detection probability $P_d^{(L)}$ depends on L , ζ_L , and γ_L . The cooperation of multiple TMTs will provide more viewing perspectives for a given target. For instance, when L is larger, it is more likely to find a pair of $\theta_{t,l}$ and θ_l which are far apart. However, the detection probability is not a monotonic increasing function of L . In the following, we give the a sufficient condition for the contribution of one TMT to be positive.

Proposition 1: For a fixed false alarm probability P_{fa} , we have $P_d^{(L+1)} > P_d^{(L)}$, if the following conditions are satisfied:

- 1) The non-central parameter with L TMTs is greater than the detection threshold, i.e., $\zeta_L > \gamma_L$;
- 2) The contribution of the $(L+1)$ th TMT is greater than the increment of the threshold, i.e.,

$$\mu_{L+1}^2 \geq \gamma_{L+1} - \gamma_L = 2\sqrt{-\frac{8}{5}\ln(4P_{fa}(1-P_{fa}))} \cdot \left(\sqrt{L + \frac{1}{2}} - \sqrt{L - \frac{1}{2}} \right) + 2. \quad (27)$$

Proof: See Appendix A.

Remark 3: In networked sensing, adding one more TMT will change the distribution of the decision statistics under both hypotheses \mathcal{H}_0 and \mathcal{H}_1 . Thus, for a given false alarm probability, one more TMT will lead to a higher detection threshold, and may not provide a higher detection probability. Consider an extreme case when the link between the target and the $(L+1)$ -th TMT is totally blocked. Under such circumstances, what the new TMT can contribute is only noise,

Algorithm 1: The TMT selection algorithm

- 1) Initialize $n = 0$, $\mathcal{S} = \emptyset$, and $\mathcal{U} = \{1, 2, \dots, M\}$.
 - 2) Find the i_n th TMT from \mathcal{U} that maximizes $\mu_{i_n}^2$, and update $\mathcal{S} = \mathcal{S} \cup \{i_n\}$, $\mathcal{U} = \mathcal{U} \cap \mathcal{S}^c$.
 - 3) $n \leftarrow n + 1$.
 - 4) Repeat 2) to 3) until the conditions in *Proposition 1* is not met.
-

causing a worse probability of detection. *Proposition 1* provides the condition with which the contribution of a new TMT ($L + 1$) is positive.

2) *TMT Selection Algorithm:* In practice, many TMTs may be around and it is unnecessary and impractical to activate all TMTs to sense one target. Thus, the selection of TMTs is critical in the networked sensing. One application of *Proposition 1* is for TMT selection. Assume there are Q TMTs available in an effective area around the target. We propose a selection algorithm, as summarized in Algorithm 1. In particular, we first calculate μ_l^2 for all available TMTs and order then in descending order. Then, the TMTs are selected based on the condition in *Proposition 1*, i.e., we keep adding new TMTs until the condition no longer holds.

IV. AI-EMPOWERED ENVIRONMENT ESTIMATION

The networked detector needs to know the second order statistics of the environment, i.e., the covariance matrices $\{\mathbf{R}_l\}_{l=1}^L$. Unfortunately, they are unknown in real application and are normally replaced by their estimates $\{\widehat{\mathbf{R}}_l\}_{l=1}^L$. For the networked sensing considered in this paper, there are two major issues for the estimation. On one hand, estimating $\{\widehat{\mathbf{R}}_l\}_{l=1}^L$ for all TMTs by the BS is challenging because moving data from TMTs to the BS can cause very heavy communication burden and lead to serious latency. One possible solution is to estimate $\{\widehat{\mathbf{R}}_l\}_{l=1}^L$ at the TMTs to avoid the heavy communication workload. However, such a distributed estimation method will require high computation workload from the TMTs, which unfortunately are computation-limited. It is necessary to develop efficient algorithms. To this end, the existing covariance matrix estimation methods, such as the widely-used sample covariance matrix (SCM) based method [6], can not be directly utilized due to its high computational complexity. Fortunately, the low-rank of the clutter makes it possible to estimate the covariance matrix by a small amount of data, which can significantly reduce the data processed at TMTs. In this section, we propose an efficient and distributed covariance estimation algorithm based on partial data.

A. Environment Estimation with Partial Data

To reduce the computation workload, the TMTs sample the clutter echo to obtain

$$\mathbf{p}_{c,l}(n) = \mathbf{\Omega}_{l,n} \mathbf{y}_{c,l}(n) \in \mathbb{C}^{p_n \times 1}, n = 1, \dots, N, \quad (28)$$

where $\mathbf{\Omega}_{l,n} \in \mathbb{C}^{p_n \times N_R}$ denotes the sampling matrix at the l th TMT in the n th subframe. In particular, if the (i, j) th entry of $\mathbf{\Omega}_{l,n}$ equals to 1, then the j th entry of $\mathbf{y}_{c,l}(n)$ is selected as the i th entry of $\mathbf{p}_{c,l}(n)$. There is only one “1” in each row of $\mathbf{\Omega}_{l,n}$ and no more than one “1” in each column such that each antenna can only be selected once. Note that the sampling matrix will take p_n values out of the N_R samples. Thus, the sparsity rate is defined as $\iota_l = \frac{\sum_{n=1}^N p_n}{NN_R}$, which represents the volume ratio between the partial data and the complete data. Note that $\mathbf{p}_{c,l}(n) \sim \mathcal{CN}(\mathbf{0}, \mathbf{\Omega}_{l,n} \mathbf{R}_l \mathbf{\Omega}_{l,n}^T)$ because $\mathbf{y}_{c,l}(n) \sim \mathcal{CN}(\mathbf{0}, \mathbf{R}_l)$.

The maximum likelihood (ML) estimate of the covariance matrix based on the partial data can be formulated as

$$\hat{\mathbf{R}}_{\text{ML},l} = \arg \max_{\mathbf{R}_l} \mathcal{L}_{\mathbf{p},l} \left(\mathbf{R}_l \mid \{\mathbf{p}_{c,l}(n)\}_{n=1}^N, \{\mathbf{\Omega}_{l,n}\}_{n=1}^N \right), \quad (29)$$

where

$$\begin{aligned} & \mathcal{L}_{\mathbf{p},l} \left(\mathbf{R}_l \mid \{\mathbf{p}_{c,l}(n)\}_{n=1}^N, \{\mathbf{\Omega}_{l,n}\}_{n=1}^N \right) \\ & \propto - \sum_{n=1}^N p_n \log \pi - \sum_{n=1}^N \left[\log \det (\mathbf{\Omega}_{l,n} \mathbf{R}_l \mathbf{\Omega}_{l,n}^T) + \mathbf{p}_{c,l}^H(n) (\mathbf{\Omega}_{l,n} \mathbf{R}_l \mathbf{\Omega}_{l,n}^T)^{-1} \mathbf{p}_{c,l}(n) \right], \end{aligned} \quad (30)$$

denotes the log-likelihood function of $\hat{\mathbf{R}}_l$ based on $\{\mathbf{p}_{c,l}(n)\}_{n=1}^N$. However, it is difficult to solve (29) directly since a closed-form solution is not available. Moreover, a solution based on an exhausted grid search in the unknown parameter space could be computationally prohibitive. This motivates us to consider an approximate estimation of \mathbf{R}_l by exploiting the partial data.

B. Expectation-maximization Algorithm

The log-likelihood function of $\hat{\mathbf{R}}_l$ based on the complete data is given as

$$\mathcal{L}_{\mathbf{y},l} \left(\hat{\mathbf{R}}_l \right) = -N \left(N_R \log \pi + \log \det \left(\hat{\mathbf{R}}_l \right) + \text{tr} \left(\hat{\mathbf{R}}_l^{-1} \hat{\mathbf{R}}_{\text{SCM},l} \right) \right), \quad (31)$$

where $\hat{\mathbf{R}}_{\text{SCM},l} \triangleq \frac{1}{N} \sum_{n=1}^N \mathbf{y}_{c,l}(n) \mathbf{y}_{c,l}^H(n)$. However, $\hat{\mathbf{R}}_{\text{SCM},l}$ is not available because the complete data $\{\mathbf{y}_{c,l}(n)\}_{n=1}^N$ is unknown. To solve the above problem, we adopt the EM algorithm, which was proposed to find an approximate ML estimation with incomplete data [30], [31]. The EM algorithm includes two steps, i.e., the expectation step (E-step) and the maximization step (M-step).

1) *E-step*: At the E-step of the t th iteration, instead finding $\mathcal{L}_{y,l}(\widehat{\mathbf{R}}_l)$, we find its conditional expectation

$$\begin{aligned}\bar{\mathcal{L}}(\widehat{\mathbf{R}}_l; \Phi_l^{(t)}) &= \mathbb{E} \left[-N \left(N_R \log \pi + \log \det(\widehat{\mathbf{R}}_l) + \text{tr}(\widehat{\mathbf{R}}_l^{-1} \widehat{\mathbf{R}}_{\text{SCM},l}) \right) \middle| \mathbf{p}_{c,l}(n), \boldsymbol{\Omega}_{l,n}, \widehat{\mathbf{R}}_l^{(t)} \right] \\ &= -N \left(N_R \log \pi + \log \det(\widehat{\mathbf{R}}_l) + \text{tr}(\widehat{\mathbf{R}}_l^{-1} \Phi_l^{(t)}) \right)\end{aligned}\quad (32)$$

where

$$\Phi_l^{(t)} = \frac{1}{N} \sum_{n=1}^N \mathbb{E} \left[\mathbf{y}_{c,l}(n) \mathbf{y}_{c,l}^H(n) \middle| \mathbf{p}_{c,l}(n), \boldsymbol{\Omega}_{l,n}, \widehat{\mathbf{R}}_l^{(t)} \right] = \frac{1}{N} \sum_{n=1}^N \mathbf{S}_n^{(t)} \quad (33)$$

and

$$\mathbf{S}_n^{(t)} \triangleq \mathbb{E} \left(\mathbf{y}_{c,l}(n) \mathbf{y}_{c,l}^H(n) \middle| \mathbf{p}_{c,l}(n), \boldsymbol{\Omega}_{l,n}, \widehat{\mathbf{R}}_l^{(t)} \right). \quad (34)$$

The following proposition gives the evaluation of $\mathbf{S}_n^{(t)}$.

Proposition 2: The conditional expectation for the covariance matrix of $\mathbf{y}_{c,l}(n)$ is given as

$$\mathbf{S}_n^{(t)} = \left(\boldsymbol{\Omega}_{l,n}^T \mathbf{p}_{c,l}(n) + \bar{\boldsymbol{\Omega}}_{l,n}^T \mathbf{k}_{c,l}^{(t)}(n) \right) \left(\boldsymbol{\Omega}_{l,n}^T \mathbf{p}_{c,l}(n) + \bar{\boldsymbol{\Omega}}_{l,n}^T \mathbf{k}_{c,l}^{(t)}(n) \right)^H + \bar{\boldsymbol{\Omega}}_{l,n}^T \boldsymbol{\Psi}_{l,n}^{(t)} \bar{\boldsymbol{\Omega}}_{l,n}, \quad (35)$$

where

$$\mathbf{k}_{c,l}^{(t)}(n) \triangleq \bar{\boldsymbol{\Omega}}_{l,n} \widehat{\mathbf{R}}_l^{(t)} \boldsymbol{\Omega}_{l,n}^T \left(\boldsymbol{\Omega}_{l,n} \widehat{\mathbf{R}}_l^{(t)} \boldsymbol{\Omega}_{l,n}^T \right)^{-1} \mathbf{p}_{c,l}(n), \quad (36)$$

$$\boldsymbol{\Psi}_{l,n}^{(t)} \triangleq \bar{\boldsymbol{\Omega}}_{l,n} \widehat{\mathbf{R}}_l^{(t)} \bar{\boldsymbol{\Omega}}_{l,n}^T - \bar{\boldsymbol{\Omega}}_{l,n} \widehat{\mathbf{R}}_l^{(t)} \boldsymbol{\Omega}_{l,n}^T \left(\boldsymbol{\Omega}_{l,n} \widehat{\mathbf{R}}_l^{(t)} \boldsymbol{\Omega}_{l,n}^T \right)^{-1} \boldsymbol{\Omega}_{l,n} \widehat{\mathbf{R}}_l^{(t)} \bar{\boldsymbol{\Omega}}_{l,n}^T, \quad (37)$$

and $\bar{\boldsymbol{\Omega}}_{l,n}$ denotes the complement selection of $\boldsymbol{\Omega}_{l,n}$.

Proof: See Appendix B.

By substituting (35) into (32), we can obtain $\bar{\mathcal{L}}(\widehat{\mathbf{R}}_l; \Phi_l^{(t)})$.

2) *M-step*: The M-step finds the update of $\widehat{\mathbf{R}}_l$ that maximizes $\bar{\mathcal{L}}(\widehat{\mathbf{R}}_l; \Phi_l^{(t)})$. The update of $\widehat{\mathbf{R}}_l$ can be obtained by setting $\partial \bar{\mathcal{L}}(\widehat{\mathbf{R}}_l; \Phi_l^{(t)}) / \partial \widehat{\mathbf{R}}_l = \mathbf{0}$, which gives

$$\widehat{\mathbf{R}}_l^{(t+1)} = \Phi_l^{(t)}. \quad (38)$$

However, $\Phi_l^{(t)}$ can be ill-conditioned if the number of samples N is smaller than the dimension N_R . As a result, the inversion operation in (15) may cause serious errors. In the following, we propose an unfolding method to solve this problem.

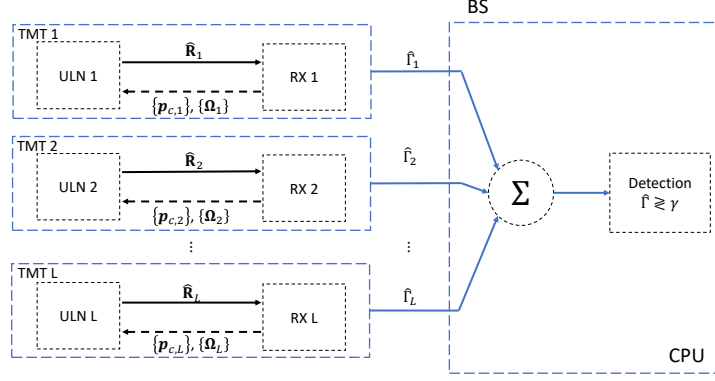


Fig. 3. The diagram of distributed EM-based networked target detection.

C. EM-Net: Unfolded EM Algorithm

1) *Penalized EM Estimator*: To tackle the above mentioned ill-conditioned issue, we consider adding a penalty term in $\bar{\mathcal{L}}(\hat{\mathbf{R}}_l; \Phi_l^{(t)})$ to improve the condition number of $\hat{\mathbf{R}}_l$. It was shown in [32] that the Kullback-Leibler (KL) divergence for Gaussian distributions, i.e.,

$$\mathcal{D}_{\text{KL}}(\hat{\mathbf{R}}_l^{-1}, \mathbf{I}) = \text{tr}(\hat{\mathbf{R}}_l^{-1}) - \log \det(\hat{\mathbf{R}}_l^{-1}) - N_{R_l}, \quad (39)$$

can effectively constrain the condition number of $\hat{\mathbf{R}}_l$. Thus, we adopt the KL divergence penalty and the penalized objective function can be given by

$$\bar{\mathcal{L}}_{\text{pen}}(\hat{\mathbf{R}}_l; \Phi_l^{(t)}) = \bar{\mathcal{L}}(\hat{\mathbf{R}}_l; \Phi_l^{(t)}) - \alpha_l^{(t)} N \mathcal{D}_{\text{KL}}(\hat{\mathbf{R}}_l^{-1}, \mathbf{I}), \quad (40)$$

where $\alpha_l^{(t)}$ denotes the penalty coefficient. The maximizer of (40) gives the update of $\hat{\mathbf{R}}_l$, i.e.,

$$\hat{\mathbf{R}}_l^{(t+1)} = (1 - \rho_l^{(t)}) \Phi_l^{(t)} + \rho_l^{(t)} \mathbf{I}, \quad (41)$$

where $\rho_l^{(t)} = \frac{\alpha_l^{(t)}}{1 + \alpha_l^{(t)}}$. (41) is a form of shrinkage estimation of the covariance matrix [32], [33], in which $\rho_l^{(t)}$ is referred to as the shrinkage coefficient. The choice of $\rho_l^{(t)}$ has been discussed based on the prior distribution of the original signal in relevant works [32], [33]. However, due to the use of partial data, the close-form solution of $\rho_l^{(t)}$ is difficult to obtain in this paper. In addition, $\rho_l^{(t)}$ changes in each iteration and the number of iterations is unpredictable, which makes the computational complexity of exhaustive searching very high. Thus, we consider utilizing determining this parameter by the following unfolding method.

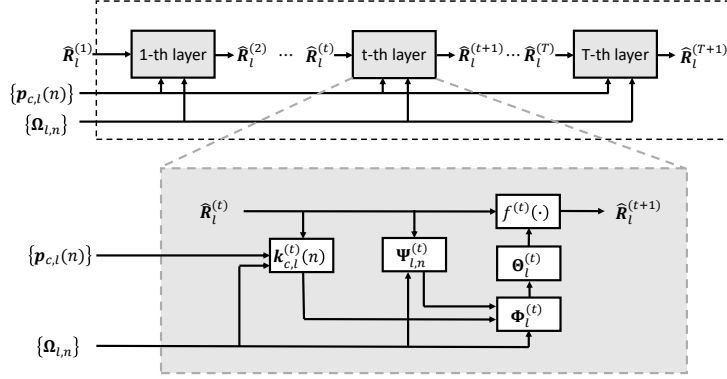


Fig. 4. The diagram of distributed EM-based networked target detection.

2) *Network Architecture*: The structure of the EM-Net is illustrated in Fig. 4, which is obtained by unfolding the EM detector and adding several trainable parameters. The network consists of T cascade layers sharing the same architecture but different trainable parameters. The input of the t th layer in the EM-Net is the output from the previous layer. The update in the t -th layer is shown in the lower part of Fig. 4 with the detailed operations as follows

$$\begin{aligned}\Phi_l^{(t)} &= \frac{1}{N} \sum_{n=1}^N \mathbf{S}_n^{(t)}, \\ \Theta_l^{(t+1)} &= (1 - \rho_l^{(t)}) \Phi_l^{(t)} + \rho_l^{(t)} \mathbf{I}, \\ \widehat{\mathbf{R}}_l^{(t+1)} &= f_l^{(t)} \left(\Theta_l^{(t+1)}; \xi_l^{(t)} \right),\end{aligned}\tag{42}$$

where the divergence-free estimator $f_l^{(t)}(\cdot)$ is constructed by

$$f_l^{(t)} \left(\Theta_l^{(t+1)}; \xi_l^{(t)} \right) = (1 - \xi_l^{(t)}) \Theta_l^{(t+1)} + \xi_l^{(t)} \widehat{\mathbf{R}}_l^{(t)}.\tag{43}$$

With the divergence-free estimator in (43) [34], the estimation results will not change dramatically after the t th layer.

Remark 4: The key difference between the EM and EM-Net is the learnable variables $\mathcal{S}_l = \{\rho_l^{(t)}, \xi_l^{(t)}\}$ in each layer. The learnable parameter $\rho_l^{(t)}$ controls the balance between estimation performance and the condition number. Another learnable parameter $\xi_l^{(t)}$ in the linear estimator $f_l^{(t)}(\cdot)$ plays an important role in constructing an appropriate divergence-free estimator. The original EM estimator in (38) can be interpreted as a special case of EM-net by setting $\rho_l^{(t)} = 0$ and $\xi_l^{(t)} = 0$.

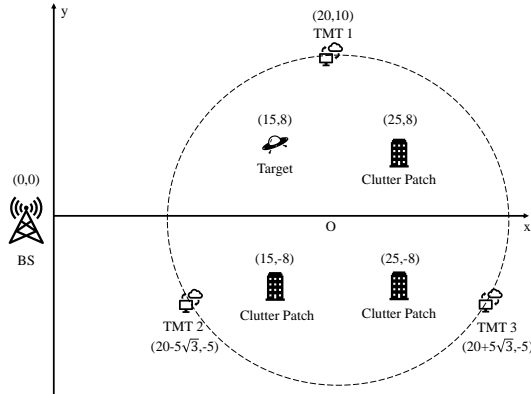


Fig. 5. The illustration of simulation scenario.

By optimizing the learnable parameters in the training process, the performance can be improved.

V. SIMULATION

In this section, we show the performance of the proposed networked sensing algorithm. Consider a PMN where the BSs are equipped with $N_T = 32$ antennas. The carrier frequency is set to 28 GHz and $\beta = 2$ [22]. The noise power σ^2 is set as -90 dBm. We set $\frac{1}{L} \sum_{l=1}^L c_{t,l}^2 / \sigma_n^2 = 8$ dB and $\frac{1}{L} \sum_{i=1}^P \sum_{l=1}^L \sigma_{l,i}^2 / \sigma_n^2 = 30$ dB unless otherwise specified. Recalling (4), the channel between the BS and k th UE is modeled as

$$\mathbf{H}_l(n) = \sqrt{N_R N_T} \sum_{i=1}^P \epsilon_{l,i}(n) \mathbf{a}_R(\theta_{l,i}) \mathbf{a}_T^H(\phi_i) \in \mathbb{C}^{N_R \times N_T}, \quad (44)$$

where $\epsilon_{l,i}(n) \sim \mathcal{CN}(0, 10^{-0.1(\kappa+\mu)})$ denotes the complex gain of the path. Here, κ is the path loss given as $\kappa = a + 10b \log_{10}(d) + \epsilon$ with d denoting the distance between the BS and the k th UE and $\epsilon \sim \mathcal{CN}(0, \sigma_\epsilon^2)$ [35]. Following [35], we set $a = 61.4$, $b = 2$, and $\sigma_\epsilon = 5.8$ dB. The channel is assumed to follow the Rician fading, where the Rician factor is set as 7 dB for LOS and 0 dB for NLOS, respectively. For a given false alarm probability P_{fa} , the detection threshold γ_L is obtained by (19). Then, 100000 Monte-Carlo trails are performed to obtain P_d .

A. Accuracy of Performance Analysis

For ease of illustration, consider a PMN with one BS and 3 TMTs, as illustrated in Fig. 5. Assume that there are one target and 3 clutter patches in the environment. We fix the locations of TMTs and the target. The coordinates of the BS, the target, the clutter patches and the

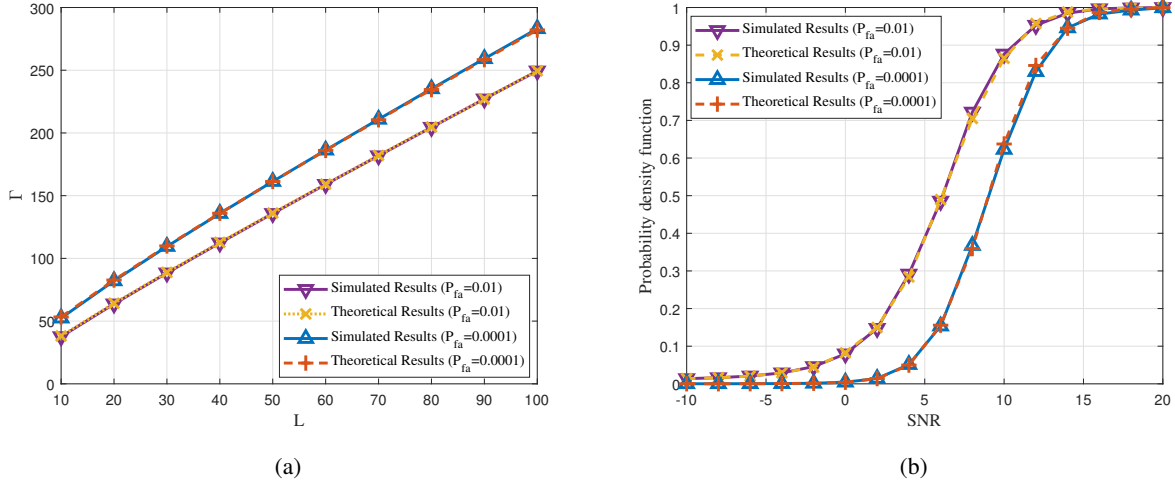


Fig. 6. Accuracy of Performance Analysis. (a) Detection Threshold γ_L ; (b) Detection Probability $P_d^{(L)}$.

TMTs are respectively given as $(0, 0)$, $(15, 8)$, $\{(25, 8), (15, -8), (25, -8)\}$, and $\{(20, 10), (20 - 5\sqrt{3}, -5), (20 + 5\sqrt{3}, -5)\}$. All coordinates are in meters. The AOD and AOA of the ST, UEs and clutter patches are obtained based on the geometric locations. For each abscissa, 5000 Monte-Carlo trials are performed.

Fig. 6 shows the accuracy of the theoretical result on the detection threshold and the detection probability. The legend ‘‘Actual Result’’ indicates that the detection threshold and the detection probability obtained by Monte-Carlo trials, while ‘‘Theoretical Result’’ represents the detection threshold and the detection probability obtained by (19) and (20). It can be observed from Fig. 6 the theoretical result fits the simulation result well.

B. Array Gain: Individual Contribution

It follows from (23) the number of antennas N_R influence μ_l^2 through SNR_l and $\cos^2 \theta_{tv,l}^\perp$. Fig. 7 shows the impact of the number of antennas N_R on SNR_l and $\cos^2 \theta_{tv,l}^\perp$ where the other settings are the same as Fig. 6. It can be observed that SNR_l grows linearly with N_R due to the array gain. However, the improvement of $\cos^2 \theta_{tv,l}^\perp$ depends on the relative locations of the target and the clutter patches as shown in Fig. 5. For example, $\cos^2 \theta_{tv,1}^\perp$ for TMT-1 increases quickly due to clear link. However, $\cos^2 \theta_{tv,3}^\perp$ for TMT-3 grows very slowly due to the two nearby clutter patches.

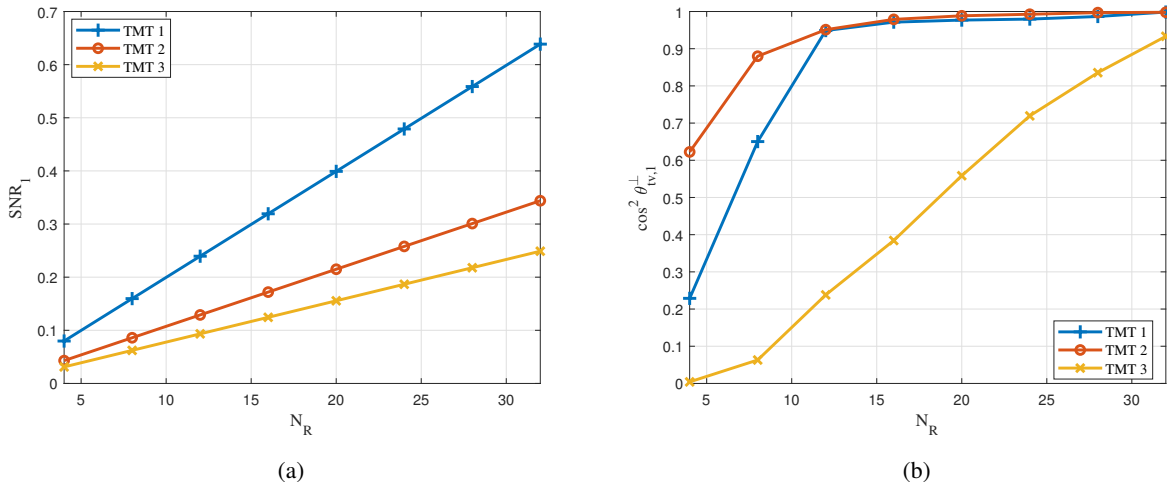


Fig. 7. Performance versus the number of antennas N_R . (a) SNR_l (b) $\cos^2 \theta_{lv,l}^\perp$.

C. Macro-Diversity

Next, we show the effect of the number of TMTs. For that purpose, we assume there are in total Q TMTs available and show the performance when L of them are selected. We set $N_R = 32$. The locations of the clutter patches are the same as those in Fig. 5. The Q TMTs are evenly located at a circle \mathcal{O} with a radius of 10m, where the coordinates of the i th TMT are given as $\left[20 + 10 \sin(2\pi \frac{i-1}{Q}), 10 \cos(2\pi \frac{i-1}{Q})\right]$, $i = 1, 2, \dots, Q$. The target is randomly generated within the circle \mathcal{O} . For each abscissa, 10000 Monte-Carlo trials are performed and we set $P_{fa} = 0.01$.

Fig. 8 shows the detection probability P_d when the best L out of Q TMTs are selected. In particular, we calculate $\{\mu_i^2\}_{i=1}^Q$ for all TMTs and arrange them in descending order, i.e., $\mu_{i(1)}^2 \geq \mu_{i(2)}^2 \geq \dots \mu_{i(Q)}^2$. Then the L TMTs with the highest μ_l^2 are selected. We have several observations. First, for a given L , P_d is an increasing function of Q due to selection diversity. However, for a given Q , P_d is not a monotonic increasing function of L . In fact, P_d will first increase, then stabilize, and finally decrease. This agrees with the discussion in Remark 3.

Next, we illustrate the performance of the proposed TMT selection algorithm. Assume L TMTs have been selected. Fig. 8b shows the difference between the increment of ζ_L and γ_L , i.e., $\mu_{L+1}^2 - (\gamma_{L+1} - \gamma_L)$. According to *Proposition 1*, adding the new TMT will benefit P_d , if $\mu_{L+1}^2 \geq \gamma_{L+1} - \gamma_L$. We can observe from Fig. 8b that $\mu_{L+1}^2 - (\gamma_{L+1} - \gamma_L)$ is positive when L is small, but as L increases, $\mu_{L+1}^2 - (\gamma_{L+1} - \gamma_L)$ decreases and then becomes negative. For example, when $Q = 12$, the cross-zero point is at $L = 10$, i.e., $\mu_{11}^2 < (\gamma_{11} - \gamma_{10})$. Therefore,

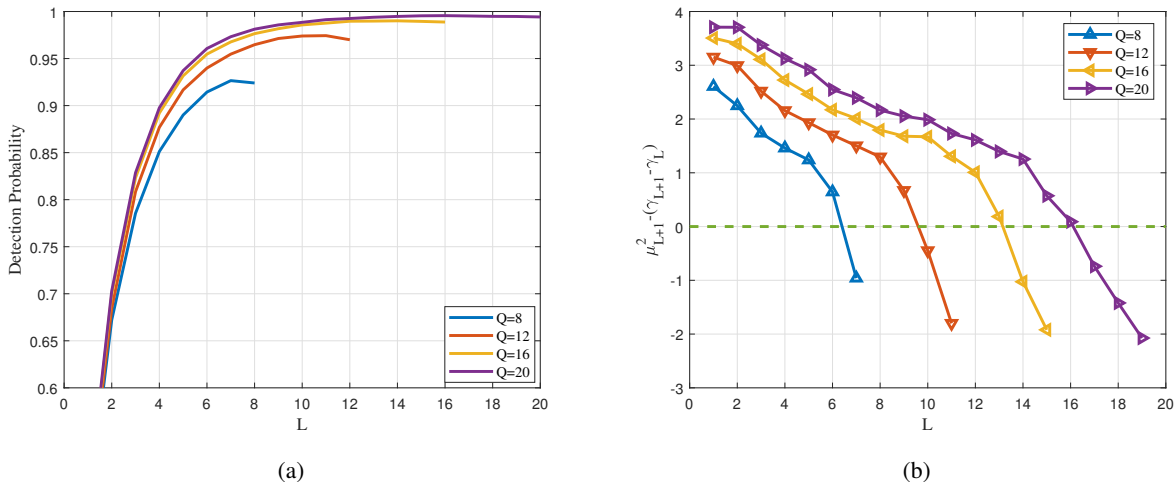


Fig. 8. Detection Probability versus the number of selected TMTs L and the number of deployed TMTs Q . (a) The effect of L with fixed Q ; (b) The difference between the increment of ζ_L and γ_L : $\mu_{L+1}^2 - (\gamma_{L+1} - \gamma_L)$.

Algorithm 1 will stop at $L = 10$. But, the optimal P_d is achieved at $L = 11$ as shown in Fig. 8a. This is because the conditions in *Proposition 1* is sufficient but not necessary. As a result, the proposed algorithm gives a conservative but relatively accurate estimation for the optimal number of TMT. Such a conservative estimation is preferred from the system complexity point of view.

D. Covariance Matrix Estimation

Next, we show the performance of the proposed EM-Net algorithm for EE. Unless otherwise specified, the number of the antennas at one TMT and the communication subframe are $N_R = 16$ and $N = 50$, respectively. We set the number of TMTs and clutter patches to be $L = 3$ and $P = 3$. The coordinates of TMTs and clutter patches are the same as those in Sec. V.A, and the target is randomly generated in the circle \mathcal{O} . Here, we set $P_{fa} = 0.01$.

For the training process, the learnable parameters are optimized by the stochastic gradient descent method. Based on the auto-differentiable machine-learning frameworks such as TensorFlow [36] and PyTorch [37], the learnable parameters can be easily trained when the loss function is determined. In our experiments, the loss function used for training is selected as

$$f_{loss} = \left(\frac{1}{N_{layer}} \sum_{i=1}^{N_{layer}} \text{SL} \left(\mathbf{R}^{(i)}, \widehat{\mathbf{R}}^{(i)}, \mathbf{a}_t \right) \right)^{-1} \quad (45)$$

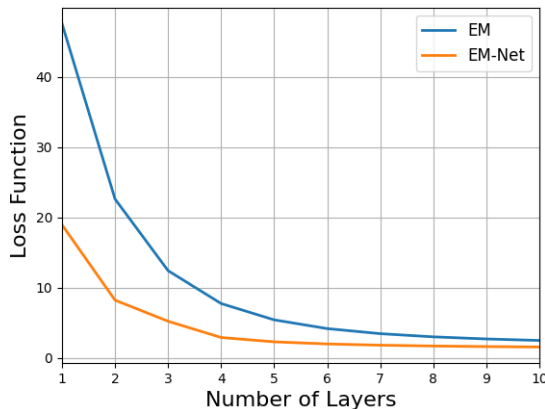


Fig. 9. Loss function of the EM-Net detector versus the number of layers.

where

$$\text{SL}(\mathbf{R}, \hat{\mathbf{R}}, \mathbf{a}_t) = \frac{\left(\mathbf{a}_t^H \hat{\mathbf{R}}^{-1} \mathbf{a}_t\right)^2}{\left(\mathbf{a}_t^H \mathbf{R}^{-1} \mathbf{a}_t\right) \left(\mathbf{a}_t^H \hat{\mathbf{R}}^{-1} \mathbf{R} \hat{\mathbf{R}}^{-1} \mathbf{a}_t\right)} \quad (46)$$

denotes the SCNR loss of the covariance estimation, i.e., the ratio between the SCNR with the estimated covariance matrix and that with the real covariance matrix, which is widely used to measure the performance of covariance estimation in radar detection [23], [28], [29], [32]. The smaller the SCNR loss is, the better the detection performance will be. The number of layers is set as $T = 10$. The batch size for each iteration is set to be equal to the total number of the communication subframes. We compare the proposed methods with the detector based on the classical SCM estimator using the complete data.

1) *Convergence Performance*: First, we analyze the convergence of the EM and EM-Net detectors. It can be observed from Fig. 9 that the EM and EM-Net detectors converge within 10 and 5 layers (iterations), respectively. Meanwhile, the EM-Net detector can achieve a lower training loss function.

2) *Effect of the number of communication subframes*: Fig. 10 shows the detection probability versus the estimation batch size. We fix $N_R = 16$, $\text{SNR} = 10$ dB, and $\iota_l = 0.5$ for all TMTs, while SCM requires the complete data. For each abscissa, 2000 Monte-Carlo trials are performed. Fig. 10 demonstrates that the detection performance will improve as the batch size increases. EM-Net outperforms EM which can achieve a better detection performance than SCM.

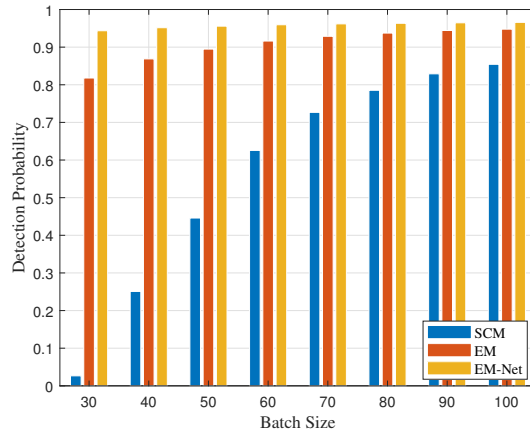


Fig. 10. Detection probability versus the batch sizes.

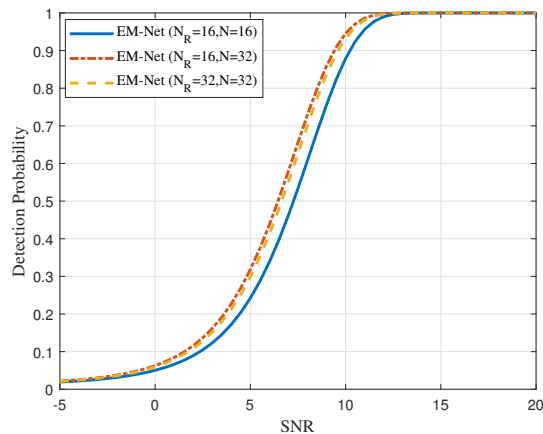


Fig. 11. Detection probability under different number of antennas on TMTs N_R .

3) *Effect of the number of antennas at TMTs:* Fig. 11 presents the detection probability with different N_R . Here we fix $\mu_l = 0.5$. Theoretically, the detection performance benefits from the increasing of N_R . However, the demand for data samples also increases as N_R increases. The comparison between “ $N_R = 16, N = 32$ ” and “ $N_R = 32, N = 32$ ” suggests that the detection performance may suffer as N_R increases if the data samples are not sufficient. This is because the number of unknown parameters to be estimated will increase with N_R . Meanwhile, the comparison between “ $N_R = 16, N = 16$ ” and “ $N_R = 32, N = 32$ ” indicates that if N_R increases with a fixed ratio between N_R and N , the detection performance will improve. Finally, the comparison of the three curves also indicates that, under certain circumstances, increasing the

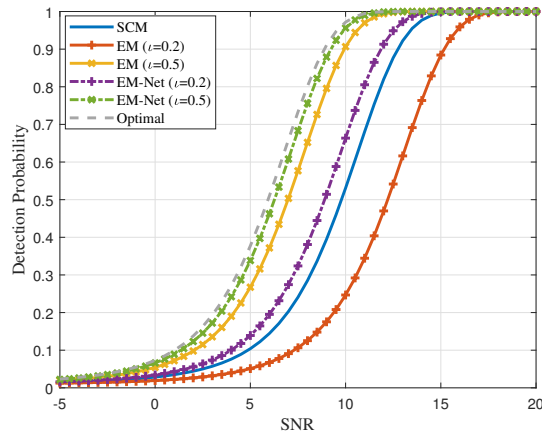


Fig. 12. Detection Probability under different sparsity rate.

data samples is more effective than deploying more antennas.

4) *Effect of the sparsity rate*: Fig. 12 depicts the detection probability versus SNR under different sparsity rate. The legend “Optimal” indicates the detection performance with real covariance matrix. For each abscissa, 2000 Monte-Carlo trials are performed. From Fig. 12, we can observe that EM-Net can outperform EM for different sparsity rates, indicating that the introduced learnable parameters improve the detection performance. Meanwhile, the detection performance of SCM is between EM and EM-Net with $\iota = 0.2$, which shows that the proposed EM-Net can achieve a better estimation performance with less data samples.

VI. CONCLUSION

This paper investigated the networked sensing in perceptive mobile networks in the presence of clutter. A networked detector was developed to exploit the macro-diversity from multiple TMTs and the array gain from multiple receive antennas. Performance analysis illustrated the impact of the macro-diversity and array gain on networked sensing. It was shown that more TMTs may not lead to better sensing performance because the added noise may out-weigh the added signal. On the other hand, multiple receive antennas donot provide diversity gain for sensing because only the LoS component is used, which is different communication. To improve the efficiency of environment estimation, an unfolded EM algorithm was proposed where only partial data are required for estimating the clutter covariance. Networked sensing brings unprecedented opportunities to exploit the well-developed infrastructure of cellular networks for sensing purpose, but at the

same time faces serious challenges in terms of communication and computing efficiency, due to the joint processing among distributed nodes over the network. This work revealed the impact of several key network parameters and demonstrated the feasibility to improve the communication and computing efficiency by machine learning empowered algorithms.

APPENDIX A

PROOF OF PROPOSITION 1

Before the proof, we define an auxiliary function $\mathcal{F}_v(a, b) = \frac{\mathcal{Q}_{v+1}(\sqrt{a}, \sqrt{b})}{\mathcal{Q}_v(\sqrt{a}, \sqrt{b})}$ and give some important theorems as follows:

Theorem 1 (Monotonicity, [38, Theorem 1]): The generalized Marcum Q-function $\mathcal{Q}_v(a, b)$ is strictly increasing in v and a for all $a \geq 0$ and $b, v > 0$, and is strictly decreasing in b for all $a, b \geq 0$ and $v > 0$.

Theorem 2: The derivative of $\log \mathcal{Q}_v(\sqrt{a}, \sqrt{b})$ with respect to a and b are respectively obtained as

$$\frac{\partial \log \mathcal{Q}_v(\sqrt{a}, \sqrt{b})}{\partial a} = \frac{1}{2} \cdot \frac{\mathcal{Q}_{v+1}(\sqrt{a}, \sqrt{b})}{\mathcal{Q}_v(\sqrt{a}, \sqrt{b})} - \frac{1}{2} \quad (47a)$$

$$\frac{\partial \log \mathcal{Q}_v(\sqrt{a}, \sqrt{b})}{\partial b} = \frac{1}{2} \cdot \frac{\mathcal{Q}_{v-1}(\sqrt{a}, \sqrt{b})}{\mathcal{Q}_v(\sqrt{a}, \sqrt{b})} - \frac{1}{2} \quad (47b)$$

Proof: (47a) and (47b) can be directly derived by the chain rule as follows:

1) (47a) can be obtained by

$$\begin{aligned} \frac{\partial \log \mathcal{Q}_v(\sqrt{a}, \sqrt{b})}{\partial b} &= \frac{\partial \log \mathcal{Q}_v(\sqrt{a}, \sqrt{b})}{\partial \mathcal{Q}_v(\sqrt{a}, \sqrt{b})} \cdot \frac{\partial \mathcal{Q}_v(\sqrt{a}, \sqrt{b})}{\partial \sqrt{a}} \cdot \frac{\partial \sqrt{a}}{\partial a} \\ &= \frac{1}{\mathcal{Q}_v(\sqrt{a}, \sqrt{b})} \cdot \left[\sqrt{a} \left(\mathcal{Q}_{v+1}(\sqrt{a}, \sqrt{b}) - \mathcal{Q}_v(\sqrt{a}, \sqrt{b}) \right) \right] \cdot \frac{1}{2\sqrt{a}} \quad (48) \\ &= \frac{1}{2} \cdot \frac{\mathcal{Q}_{v+1}(\sqrt{a}, \sqrt{b})}{\mathcal{Q}_v(\sqrt{a}, \sqrt{b})} - \frac{1}{2}. \end{aligned}$$

2) (47b) can be obtained by

$$\begin{aligned} \frac{\partial \log \mathcal{Q}_v(\sqrt{a}, \sqrt{b})}{\partial b} &= \frac{\partial \log \mathcal{Q}_v(\sqrt{a}, \sqrt{b})}{\partial \mathcal{Q}_v(\sqrt{a}, \sqrt{b})} \cdot \frac{\partial \mathcal{Q}_v(\sqrt{a}, \sqrt{b})}{\partial \sqrt{b}} \cdot \frac{\partial \sqrt{b}}{\partial b} \\ &= \frac{1}{\mathcal{Q}_v(\sqrt{a}, \sqrt{b})} \cdot \left[\sqrt{b} \left(\mathcal{Q}_{v-1}(\sqrt{a}, \sqrt{b}) - \mathcal{Q}_v(\sqrt{a}, \sqrt{b}) \right) \right] \cdot \frac{1}{2\sqrt{b}} \quad (49) \\ &= \frac{1}{2} \cdot \frac{\mathcal{Q}_{v-1}(\sqrt{a}, \sqrt{b})}{\mathcal{Q}_v(\sqrt{a}, \sqrt{b})} - \frac{1}{2}. \end{aligned}$$

Theorem 3: The auxiliary function $b \mapsto \mathcal{F}_v(a, b)$ is monotonically decreasing for $a \geq b > 0$. ■

Proof: For all $a \geq 0$ and $b, v > 0$, since $\mathcal{Q}_v(a, b)$ is strictly increasing in v [38, Theorem 1], we have $\mathcal{Q}_v(\sqrt{a}, \sqrt{b}) < \mathcal{Q}_{v+1}(\sqrt{a}, \sqrt{b})$. Meanwhile, in view of [39, Theorem 3.1(b)], the function $v \mapsto \mathcal{Q}_{v+1}(\sqrt{a}, \sqrt{b}) - \mathcal{Q}_v(\sqrt{a}, \sqrt{b})$ is strictly decreasing on $(0, +\infty)$ for $a \geq b > 0$. Thus, we have

$$\mathcal{Q}_{v+1}(\sqrt{a}, \sqrt{b}) - \mathcal{Q}_v(\sqrt{a}, \sqrt{b}) < \mathcal{Q}_v(\sqrt{a}, \sqrt{b}) - \mathcal{Q}_{v-1}(\sqrt{a}, \sqrt{b}). \quad (50)$$

We know that $\frac{x}{y} > \frac{x+u}{y+v}$ for all $0 < y < x$ and $0 < u < v$. Thus, invoking $x = \mathcal{Q}_v(\sqrt{a}, \sqrt{b})$, $y = \mathcal{Q}_{v-1}(\sqrt{a}, \sqrt{b})$, $u = \mathcal{Q}_{v+1}(\sqrt{a}, \sqrt{b}) - \mathcal{Q}_v(\sqrt{a}, \sqrt{b})$, and $v = \mathcal{Q}_v(\sqrt{a}, \sqrt{b}) - \mathcal{Q}_{v-1}(\sqrt{a}, \sqrt{b})$, we have

$$\mathcal{F}_v(a, b) = \frac{\mathcal{Q}_v(\sqrt{a}, \sqrt{b}) + \left(\mathcal{Q}_{v+1}(\sqrt{a}, \sqrt{b}) - \mathcal{Q}_v(\sqrt{a}, \sqrt{b}) \right)}{\mathcal{Q}_{v-1}(\sqrt{a}, \sqrt{b}) + \left(\mathcal{Q}_v(\sqrt{a}, \sqrt{b}) - \mathcal{Q}_{v-1}(\sqrt{a}, \sqrt{b}) \right)} < \mathcal{F}_{v-1}(a, b). \quad (51)$$

Theorem 4: For all $a, b \geq 0$, $\Delta a, \Delta b > 0$, and $v > 0$, we have

$$\log \mathcal{Q}_v(\sqrt{a + \Delta a}, \sqrt{b}) - \log \mathcal{Q}_v(\sqrt{a}, \sqrt{b}) \geq \left(\frac{1}{2} \cdot \frac{\mathcal{Q}_{v+1}(\sqrt{a + \Delta a}, \sqrt{b})}{\mathcal{Q}_v(\sqrt{a + \Delta a}, \sqrt{b})} - \frac{1}{2} \right) \Delta a, \quad (52a)$$

$$\log \mathcal{Q}_v(\sqrt{a}, \sqrt{b + \Delta b}) - \log \mathcal{Q}_v(\sqrt{a}, \sqrt{b}) \geq \left(\frac{1}{2} \cdot \frac{\mathcal{Q}_{v-1}(\sqrt{a}, \sqrt{b + \Delta b})}{\mathcal{Q}_v(\sqrt{a}, \sqrt{b + \Delta b})} - \frac{1}{2} \right) \Delta b, \quad (52b)$$

Proof: Since $a \mapsto \mathcal{Q}_v(\sqrt{a}, \sqrt{b})$ and $b \mapsto \mathcal{Q}_v(\sqrt{a}, \sqrt{b})$ are both log-concave for all $a, b \geq 0$ and $v > 0$ [38], [39], the function $a \mapsto \log \mathcal{Q}_v(\sqrt{a}, \sqrt{b})$ and $b \mapsto \log \mathcal{Q}_v(\sqrt{a}, \sqrt{b})$ are both concave.

We begin with proving (52a). According to mean value theorem [40], there exists a point ξ in $(a, a + \Delta a)$ such that

$$\log \mathcal{Q}_v(\sqrt{a + \Delta a}, \sqrt{b}) - \log \mathcal{Q}_v(\sqrt{a}, \sqrt{b}) = \frac{\partial \log \mathcal{Q}_v(\sqrt{a}, \sqrt{b})}{\partial a} \Big|_{a=\xi} \cdot \Delta a. \quad (53)$$

From the property of the concave function, we have

$$\frac{\partial \log \mathcal{Q}_v(\sqrt{a}, \sqrt{b})}{\partial a} \Big|_{a=\xi} \geq \frac{\partial \log \mathcal{Q}_v(\sqrt{a}, \sqrt{b})}{\partial a} \Big|_{a=a+\Delta a}. \quad (54)$$

In view of (53) and (54), the inequality (52a) is proved. Similarly, the inequality (52b) can be obtained. ■

Next, we will prove Proposition 1. Given $P_d^{(L+1)} > 0$ and $P_d^{(L)} > 0$, we have

$$\log \frac{P_d^{(L+1)}}{P_d^{(L)}} = \log \mathcal{Q}_{L+1} \left(\sqrt{\zeta_{L+1}}, \sqrt{\gamma_{L+1}} \right) - \log \mathcal{Q}_L \left(\sqrt{\zeta_L}, \sqrt{\gamma_L} \right) = \mathcal{A}_1 + \mathcal{A}_2 + \mathcal{A}_3, \quad (55)$$

where

$$\begin{aligned}
\mathcal{A}_1 &= \log \mathcal{Q}_{L+1} \left(\sqrt{\zeta_{L+1}}, \sqrt{\gamma_{L+1}} \right) - \log \mathcal{Q}_{L+1} \left(\sqrt{\zeta_{L+1}}, \sqrt{\gamma_L} \right), \\
\mathcal{A}_2 &= \log \mathcal{Q}_{L+1} \left(\sqrt{\zeta_{L+1}}, \sqrt{\gamma_L} \right) - \log \mathcal{Q}_L \left(\sqrt{\zeta_{L+1}}, \sqrt{\gamma_L} \right), \\
\mathcal{A}_3 &= \log \mathcal{Q}_L \left(\sqrt{\zeta_{L+1}}, \sqrt{\gamma_L} \right) - \log \mathcal{Q}_L \left(\sqrt{\zeta_L}, \sqrt{\gamma_L} \right).
\end{aligned} \tag{56}$$

Recalling (17), the detection statistic follows a non-central chi-square distribution under \mathcal{H}_1 . \mathcal{A}_1 , \mathcal{A}_2 , and \mathcal{A}_3 represent the increment of detection probability with respect to the detection threshold γ_L , the degree of detection statistic L , and the non-central parameter ζ_L , respectively. By observing *Theorem 1*, we have that $\mathcal{A}_2 \geq 0$, $\mathcal{A}_3 \geq 0$, and $\mathcal{A}_1 < 0$. The first two inequalities hold because increasing the DOF and the non-central parameter of Γ_L will increase the detection probability. However, a larger γ_L will decrease $P_d^{(L)}$, which leads to $\mathcal{A}_1 < 0$.

By applying *Theorem 4*, we have

$$\begin{aligned}
\mathcal{A}_1 &\geq \left(\frac{1}{2} \cdot \frac{\mathcal{Q}_L(\sqrt{\zeta_{L+1}}, \sqrt{\gamma_{L+1}})}{\mathcal{Q}_{L+1}(\sqrt{\zeta_{L+1}}, \sqrt{\gamma_{L+1}})} - \frac{1}{2} \right) (\gamma_{L+1} - \gamma_L) \\
&= -\frac{1}{2} \left(1 - \frac{1}{\mathcal{F}_L(\zeta_{L+1}, \gamma_{L+1})} \right) (\gamma_{L+1} - \gamma_L)
\end{aligned} \tag{57}$$

and

$$\mathcal{A}_3 \geq \left(\frac{1}{2} \cdot \frac{\mathcal{Q}_{L+1}(\sqrt{\zeta_{L+1}}, \sqrt{\gamma_L})}{\mathcal{Q}_L(\sqrt{\zeta_{L+1}}, \sqrt{\gamma_L})} - \frac{1}{2} \right) \mu_{L+1}^2 = \frac{1}{2} (\mathcal{F}_L(\zeta_{L+1}, \gamma_L) - 1) \mu_{L+1}^2 \tag{58}$$

Recalling the conditions 1) and 2) in *Proposition 1*, we have $\zeta_{L+1} > \gamma_{L+1} > 0$ and $\zeta_{L+1} > \gamma_L > 0$, which means that *Theorem 3* hold true for both $\mathcal{F}_L(\zeta_{L+1}, \gamma_{L+1})$ and $\mathcal{F}_L(\zeta_{L+1}, \gamma_L)$. Applying *Theorem 3* yields $\mathcal{F}_L(\zeta_{L+1}, \gamma_{L+1}) < \mathcal{F}_L(\zeta_{L+1}, \gamma_L)$. Thus, we have

$$\begin{aligned}
&\mathcal{F}_L(\zeta_{L+1}, \gamma_L) \mathcal{F}_L(\zeta_{L+1}, \gamma_{L+1}) - 2\mathcal{F}_L(\zeta_{L+1}, \gamma_{L+1}) + 1 \\
&\geq \mathcal{F}_L^2(\zeta_{L+1}, \gamma_{L+1}) - 2\mathcal{F}_L(\zeta_{L+1}, \gamma_{L+1}) + 1 = (\mathcal{F}_L(\zeta_{L+1}, \gamma_{L+1}) - 1)^2 \geq 0,
\end{aligned} \tag{59}$$

By rearranging (59), we have

$$1 - \frac{1}{\mathcal{F}_L(\zeta_{L+1}, \gamma_{L+1})} \leq \mathcal{F}_L(\zeta_{L+1}, \gamma_L) - 1 \tag{60}$$

From *Theorem 1*, we have $\mathcal{F}_v(a, b) > 1$, such that $1 - \frac{1}{\mathcal{F}_L(\zeta_{L+1}, \gamma_{L+1})} > 0$ and $\mathcal{F}_L(\zeta_{L+1}, \gamma_L) - 1 > 0$. Recalling (27) and (60), we have $\mathcal{A}_1 + \mathcal{A}_3 \geq 0$. Recalling that $\mathcal{A}_2 \geq 0$. Therefore, we have

$$\log \frac{P_d^{(L+1)}}{P_d^{(L)}} = \mathcal{A}_1 + \mathcal{A}_2 + \mathcal{A}_3 \geq 0. \tag{61}$$

That is $P_d^{(L+1)} > P_d^{(L)}$, which completes the proof. ■

APPENDIX B

PROOF OF PROPOSITION 2

First, we define $\mathbf{Q}_{l,n} = \left[\mathbf{\Omega}_{l,n}^T, \bar{\mathbf{\Omega}}_{l,n}^T \right]^T$. It can be validated that $\mathbf{Q}_{l,n}^T \mathbf{Q}_{l,n} = \mathbf{I}$. Then we have

$$\begin{aligned} \Xi_n &= \mathbb{E} \left(\mathbf{Q}_{l,n} \mathbf{y}_{c,l}(n) \mathbf{y}_{c,l}^H(n) \mathbf{Q}_{l,n}^T \mid \mathbf{p}_{c,l}(n), \mathbf{\Omega}_{l,n}, \hat{\mathbf{R}}_l^{(t)} \right) \\ &= \begin{bmatrix} \mathbf{p}_{c,l} \mathbf{p}_{c,l}^H & \mathbf{p}_{c,l} \mathbb{E} \left(\mathbf{y}_{c,l}^H(n) \bar{\mathbf{\Omega}}_{l,n}^T \mid \mathbf{p}_{c,l}(n), \mathbf{\Omega}_{l,n}, \hat{\mathbf{R}}_l^{(t)} \right) \\ \mathbb{E} \left(\bar{\mathbf{\Omega}}_{l,n} \mathbf{y}_{c,l}(n) \mid \mathbf{p}_{c,l}(n), \mathbf{\Omega}_{l,n}, \hat{\mathbf{R}}_l^{(t)} \right) \mathbf{p}_{c,l}^H & \mathbb{E} \left(\bar{\mathbf{\Omega}}_{l,n} \mathbf{y}_{c,l}(n) \mathbf{y}_{c,l}^H(n) \bar{\mathbf{\Omega}}_{l,n}^T \mid \mathbf{p}_{c,l}(n), \mathbf{\Omega}_{l,n}, \hat{\mathbf{R}}_l^{(t)} \right) \end{bmatrix}. \end{aligned} \quad (62)$$

Since $\bar{\mathbf{\Omega}}_{l,n} \mathbf{y}_{c,l}(n)$ follows the Gaussian distribution, we have [41]

$$\mathbb{E} \left(\bar{\mathbf{\Omega}}_{l,n} \mathbf{y}_{c,l}(n) \mid \mathbf{p}_{c,l}(n), \mathbf{\Omega}_{l,n}, \hat{\mathbf{R}}_l^{(t)} \right) = \mathbf{k}_{c,l}^{(t)}(n), \quad (63)$$

$$\mathbb{E} \left(\bar{\mathbf{\Omega}}_{l,n} \mathbf{y}_{c,l}(n) \mathbf{y}_{c,l}^H(n) \bar{\mathbf{\Omega}}_{l,n}^T \mid \mathbf{p}_{c,l}(n), \mathbf{\Omega}_{l,n}, \hat{\mathbf{R}}_l^{(t)} \right) = \mathbf{\Psi}_{l,n}^{(t)} + \mathbf{k}_{c,l}^{(t)}(n) \mathbf{k}_{c,l}^{(t),H}(n). \quad (64)$$

By substituting (63) and (64) into (62), we have

$$\mathbf{S}_n^{(t)} = \mathbf{Q}_{l,n}^T \Xi_n \mathbf{Q}_{l,n} = \left(\mathbf{\Omega}_{l,n}^T \mathbf{p}_{c,l}(n) + \bar{\mathbf{\Omega}}_{l,n}^T \mathbf{k}_{c,l}^{(t)}(n) \right) \left(\mathbf{\Omega}_{l,n}^T \mathbf{p}_{c,l}(n) + \bar{\mathbf{\Omega}}_{l,n}^T \mathbf{k}_{c,l}^{(t)}(n) \right)^H + \bar{\mathbf{\Omega}}_{l,n}^T \mathbf{\Psi}_{l,n}^{(t)} \bar{\mathbf{\Omega}}_{l,n}.$$

REFERENCES

- [1] Y. Cui, F. Liu, X. Jing, and J. Mu, "Integrating sensing and communications for ubiquitous iot: Applications, trends and challenges," *arXiv preprint, arXiv:2104.11457*, 2021.
- [2] K. Chen, D. Zhang, L. Yao, B. Guo, Z. Yu, and Y. Liu, "Deep learning for sensor-based human activity recognition: Overview, challenges, and opportunities," *ACM Comput. Surv.*, vol. 54, no. 4, may 2021.
- [3] Q. Huang, H. Chen, and Q. Zhang, "Joint design of sensing and communication systems for smart homes," *IEEE Network*, vol. 34, no. 6, pp. 191–197, 2020.
- [4] A. Moreira, P. Prats-Iraola, M. Younis, G. Krieger, I. Hajnsek, and K. P. Papathanassiou, "A tutorial on synthetic aperture radar," *IEEE Geoscience and Remote Sensing Magazine*, vol. 1, no. 1, pp. 6–43, 2013.
- [5] A. Zhang, M. L. Rahman, X. Huang, Y. J. Guo, S. Chen, and R. W. Heath, "Perceptive mobile networks: Cellular networks with radio vision via joint communication and radar sensing," *IEEE Vehicular Technology Magazine*, vol. 16, no. 2, pp. 20–30, 2021.
- [6] F. Liu, C. Masouros, A. P. Petropulu, H. Griffiths, and L. Hanzo, "Joint radar and communication design: Applications, state-of-the-art, and the road ahead," *IEEE Transactions on Communications*, vol. 68, no. 6, pp. 3834–3862, 2020.
- [7] F. Liu, Y. Cui, C. Masouros, J. Xu, T. X. Han, Y. C. Eldar, and S. Buzzi, "Integrated sensing and communications: Towards dual-functional wireless networks for 6g and beyond," *IEEE Journal on Selected Areas in Communications*, pp. 1–1, 2022.
- [8] J. A. Zhang, F. Liu, C. Masouros, R. W. Heath, Z. Feng, L. Zheng, and A. Petropulu, "An overview of signal processing techniques for joint communication and radar sensing," *IEEE Journal of Selected Topics in Signal Processing*, vol. 15, no. 6, pp. 1295–1315, 2021.

- [9] F. Liu, Y. Cui, C. Masouros, J. Xu, T. X. Han, Y. C. Eldar, and S. Buzzi, "Integrated sensing and communications: Towards dual-functional wireless networks for 6g and beyond," 2021.
- [10] D. Bharadia, E. McMillin, and S. Katti, "Full duplex radios," in *Proceedings of the ACM SIGCOMM 2013 conference on SIGCOMM*, 2013, pp. 375–386.
- [11] A. Sabharwal, P. Schniter, D. Guo, D. W. Bliss, S. Rangarajan, and R. Wichman, "In-band full-duplex wireless: Challenges and opportunities," *IEEE Journal on selected areas in communications*, vol. 32, no. 9, pp. 1637–1652, 2014.
- [12] F. Dong, F. Liu, Y. Cui, W. Wang, K. Han, and Z. Wang, "Sensing as a service in 6g perceptive networks: A unified framework for isac resource allocation," *arXiv preprint arXiv:2202.09969*, 2022.
- [13] X. Wang, Z. Fei, J. A. Zhang, J. Huang, and J. Yuan, "Constrained utility maximization in dual-functional radar-communication multi-uav networks," *IEEE Transactions on Communications*, vol. 69, no. 4, pp. 2660–2672, 2021.
- [14] L. Xie, P. Wang, S. Song, and K. B. Letaief, "Perceptive mobile network with distributed target monitoring terminals: Leaking communication energy for sensing," *arXiv preprint arXiv:2112.14391*, 2021.
- [15] M. L. Rahman, J. A. Zhang, X. Huang, Y. J. Guo, and R. W. Heath, "Framework for a perceptive mobile network using joint communication and radar sensing," *IEEE Transactions on Aerospace and Electronic Systems*, vol. 56, no. 3, pp. 1926–1941, 2020.
- [16] S. Wang, Y. Hou, F. Gao, and X. Ji, "A novel iot access architecture for vehicle monitoring system," in *2016 IEEE 3rd World Forum on Internet of Things (WF-IoT)*, 2016, pp. 639–642.
- [17] S. Sun, A. P. Petropulu, and W. U. Bajwa, "Target estimation in colocated mimo radar via matrix completion," in *2013 IEEE International Conference on Acoustics, Speech and Signal Processing*. IEEE, 2013, pp. 4144–4148.
- [18] S. Sun, W. U. Bajwa, and A. P. Petropulu, "Mimo-mc radar: A mimo radar approach based on matrix completion," *IEEE Transactions on Aerospace and Electronic Systems*, vol. 51, no. 3, pp. 1839–1852, 2015.
- [19] B. Li, A. P. Petropulu, and W. Trappe, "Optimum co-design for spectrum sharing between matrix completion based mimo radars and a mimo communication system," *IEEE Transactions on Signal Processing*, vol. 64, no. 17, pp. 4562–4575, 2016.
- [20] E. Fishler, A. Haimovich, R. Blum, D. Chizhik, L. Cimini, and R. Valenzuela, "Mimo radar: an idea whose time has come," in *Proceedings of the 2004 IEEE Radar Conference (IEEE Cat. No.04CH37509)*, 2004, pp. 71–78.
- [21] B. Friedlander, "On signal models for mimo radar," *IEEE Transactions on Aerospace and Electronic Systems*, vol. 48, no. 4, pp. 3655–3660, 2012.
- [22] M. R. Akdeniz, Y. Liu, M. K. Samimi, S. Sun, S. Rangan, T. S. Rappaport, and E. Erkip, "Millimeter wave channel modeling and cellular capacity evaluation," *IEEE journal on selected areas in communications*, vol. 32, no. 6, pp. 1164–1179, 2014.
- [23] L. Xie, Z. He, J. Tong, and W. Zhang, "A recursive angle-doppler channel selection method for reduced-dimension space-time adaptive processing," *IEEE Transactions on Aerospace and Electronic Systems*, vol. 56, no. 5, pp. 3985–4000, 2020.
- [24] F. Robey, D. Fuhrmann, E. Kelly, and R. Nitzberg, "A cfar adaptive matched filter detector," *IEEE Transactions on Aerospace and Electronic Systems*, vol. 28, no. 1, pp. 208–216, 1992.
- [25] E. J. Kelly and K. M. Forsythe, "Adaptive detection and parameter estimation for multidimensional signal models," Massachusetts Inst of Tech Lexington Lincoln Lab, Tech. Rep., 1989.
- [26] D. Shnidman, "The calculation of the probability of detection and the generalized marcum q-function," *IEEE Transactions on Information Theory*, vol. 35, no. 2, pp. 389–400, 1989.
- [27] J. Omura and T. Kailath, "Some useful probability distributions," STANFORD UNIV CA STANFORD ELECTRONICS LABS, Tech. Rep., 1965.
- [28] W. L. Melvin, "A STAP overview," *IEEE Aerospace and Electronic Systems Magazine*, vol. 19, no. 1, pp. 19–35, Jan 2004.

- [29] I. S. Reed, J. D. Mallett, and L. E. Brennan, "Rapid Convergence Rate in Adaptive Arrays," *IEEE Transactions on Aerospace and Electronic Systems*, vol. AES-10, no. 6, pp. 853–863, Nov 1974.
- [30] A. P. Dempster, N. M. Laird, and D. B. Rubin, "Maximum likelihood from incomplete data via the em algorithm," *Journal of the Royal Statistical Society: Series B (Methodological)*, vol. 39, no. 1, pp. 1–22, 1977.
- [31] C. M. Bishop and N. M. Nasrabadi, *Pattern recognition and machine learning*. Springer, 2006, vol. 4, no. 4.
- [32] L. Xie, Z. He, J. Tong, T. Liu, J. Li, and J. Xi, "Regularized covariance estimation for polarization radar detection in compound gaussian sea clutter," *IEEE Transactions on Geoscience and Remote Sensing*, vol. 60, pp. 1–16, 2022.
- [33] Y. Chen, A. Wiesel, Y. C. Eldar, and A. O. Hero, "Shrinkage algorithms for mmse covariance estimation," *IEEE Transactions on Signal Processing*, vol. 58, no. 10, pp. 5016–5029, 2010.
- [34] J. Ma and L. Ping, "Orthogonal amp," *IEEE Access*, vol. 5, pp. 2020–2033, 2017.
- [35] M. R. Akdeniz, Y. Liu, M. K. Samimi, S. Sun, S. Rangan, T. S. Rappaport, and E. Erkip, "Millimeter wave channel modeling and cellular capacity evaluation," *IEEE J. Sel. Areas Commun.*, vol. 32, no. 6, pp. 1164–1179, 2014.
- [36] M. Abadi, A. Agarwal, P. Barham, E. Brevdo, Z. Chen, C. Citro, G. S. Corrado, A. Davis, J. Dean, M. Devin *et al.*, "Tensorflow: Large-scale machine learning on heterogeneous distributed systems," *arXiv preprint arXiv:1603.04467*, 2016.
- [37] A. Paszke, S. Gross, S. Chintala, G. Chanan, E. Yang, Z. DeVito, Z. Lin, A. Desmaison, L. Antiga, and A. Lerer, "Automatic differentiation in pytorch," 2017.
- [38] Y. Sun, Á. Baricz, and S. Zhou, "On the monotonicity, log-concavity, and tight bounds of the generalized marcum and nuttall q -functions," *IEEE Transactions on Information Theory*, vol. 56, no. 3, pp. 1166–1186, 2010.
- [39] Y. Sun and Á. Baricz, "Inequalities for the generalized marcum q -function," *Applied Mathematics and Computation*, vol. 203, no. 1, pp. 134–141, 2008.
- [40] P. Sahoo and T. Riedel, *Mean value theorems and functional equations*. World Scientific, 1998.
- [41] S. M. Kay, *Fundamentals of statistical signal processing: estimation theory*. Prentice-Hall, Inc., 1993.